Poly(dopamine)-coated TiO_2/SiO_2 resonators for the non-plasmonic SERS detection of organic analytes

Autchariya Boontanom,[1] Leonardo Moscolari,[2] Erika Kozma,[2] Michele Speziani,[3,4] Ivano Alessandri,[1,4,5] Francesco Galeotti,[2] Irene Vassalini[1,4,5]*

[1] Department of Information Engineering, University of Brescia, via Branze 38, 25123 Brescia, Italy

[2] Istituto di Scienze e Tecnologie Chimiche "Giulio Natta", Consiglio Nazionale delle Ricerche, Via A. Corti 12, 20133 Milano, Italy

[3] Department of Mechanical and Industrial Engineering, University of Brescia, via Branze 38, 25123 Brescia, Italy

[4] INSTM, UdR Brescia, Italy

[5] INO-CNR, Via Branze 38, 25123 Brescia, Italy

S1. Optical and morphological characterization

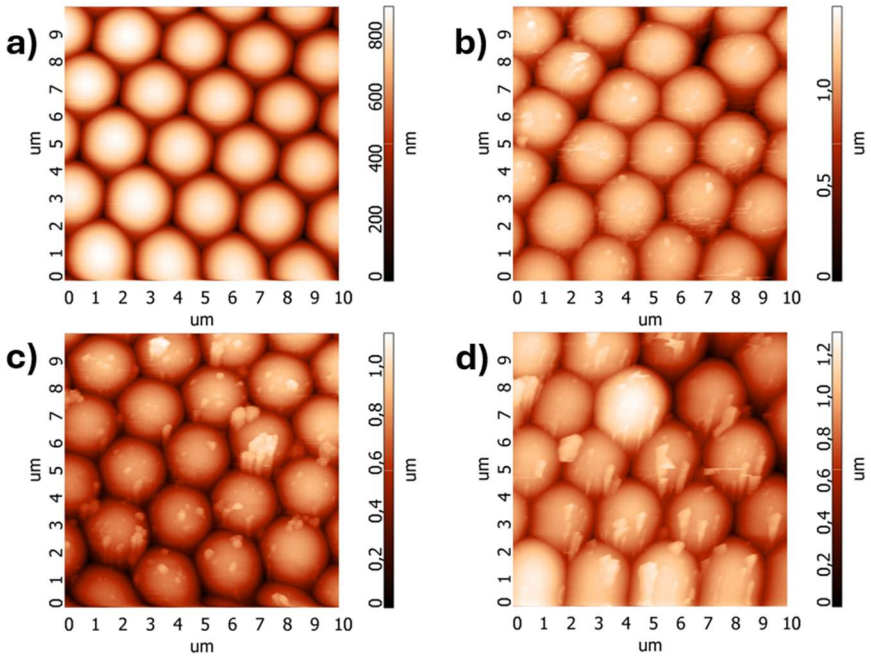

Figure S 1.1. AFM images of monolayer T-rex samples before (a) and after incubation with dopamine hydrochloride for 1 h (b), 2 h (c) and 4 h (d).

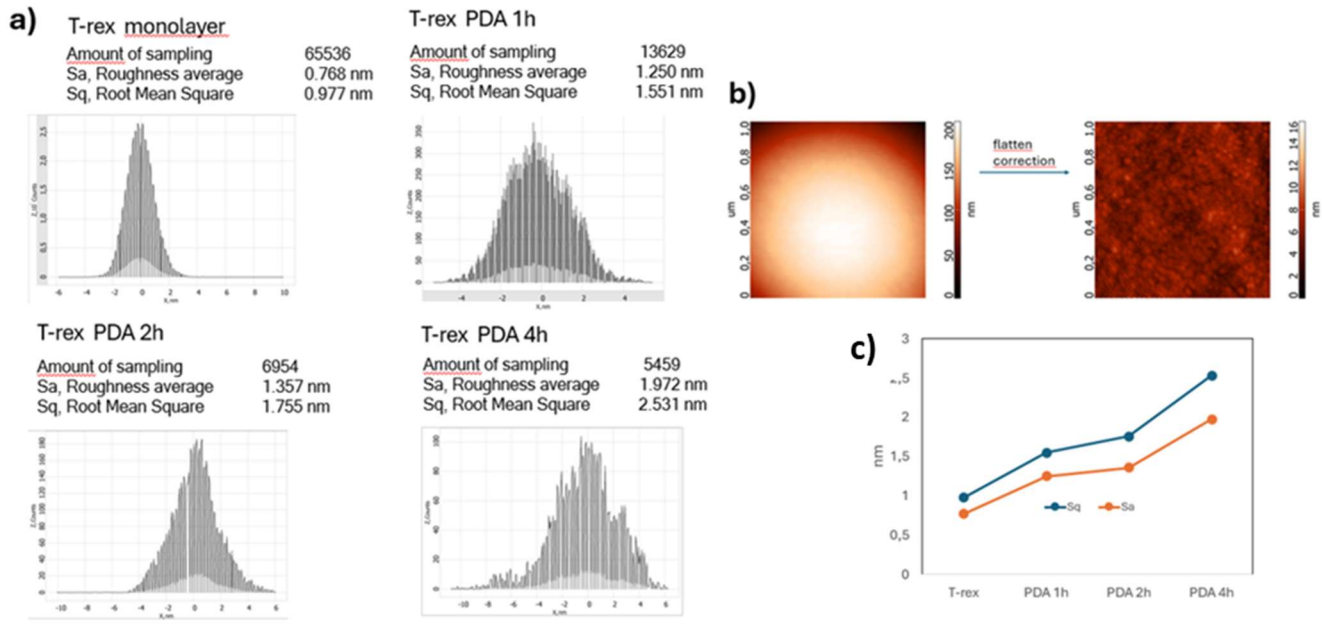

Figure S1.2. a) Roughness analysis of monolayer T-rex samples before and after incubation with dopamine hydrochloride for 1, 2 and 4 h. Data collected from 1.0 x 1.0 um AFM scans of a single T-rex sphere after flatten correction. b) Example of flatten correction used for roughness analysis of nude T-rex sample. c) Evolution of roughness average (cyan) and root mean square (orange) values.

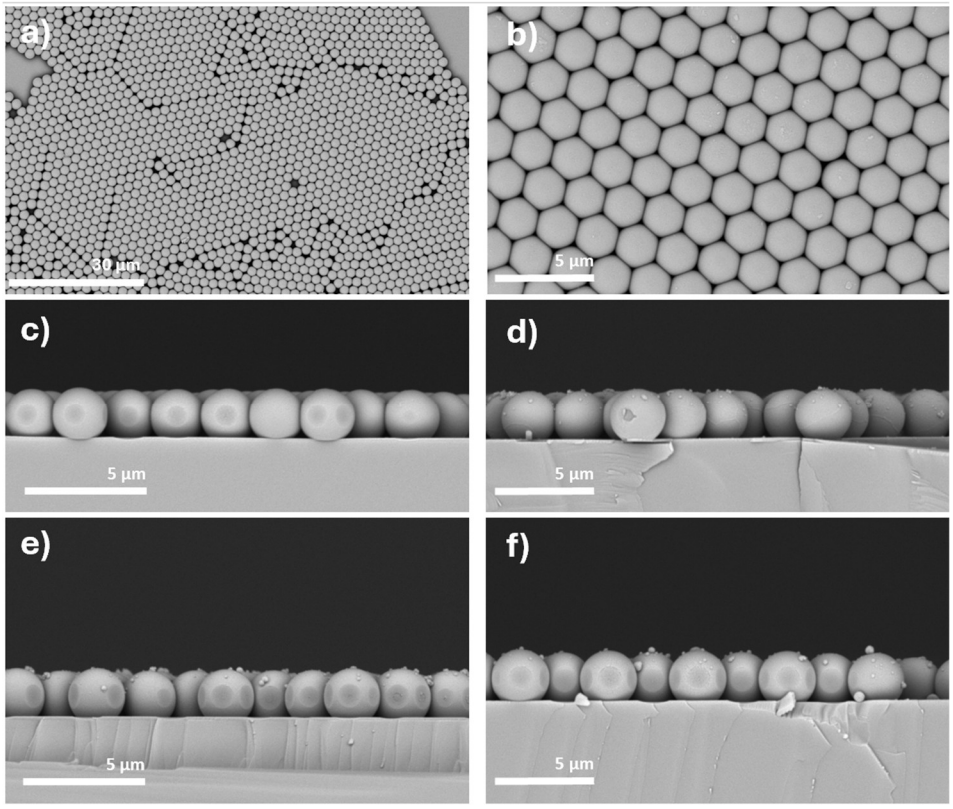

Figure S1.3. SEM images of T-rex monolayers. a) and b) Top view images of monolayer T-rex at different magnifications; c), d), e), f) Section view images of T-rex monolayer before (c) and after polydopamine coating for 1 h (d), 2 h (e), and 4 h (f).

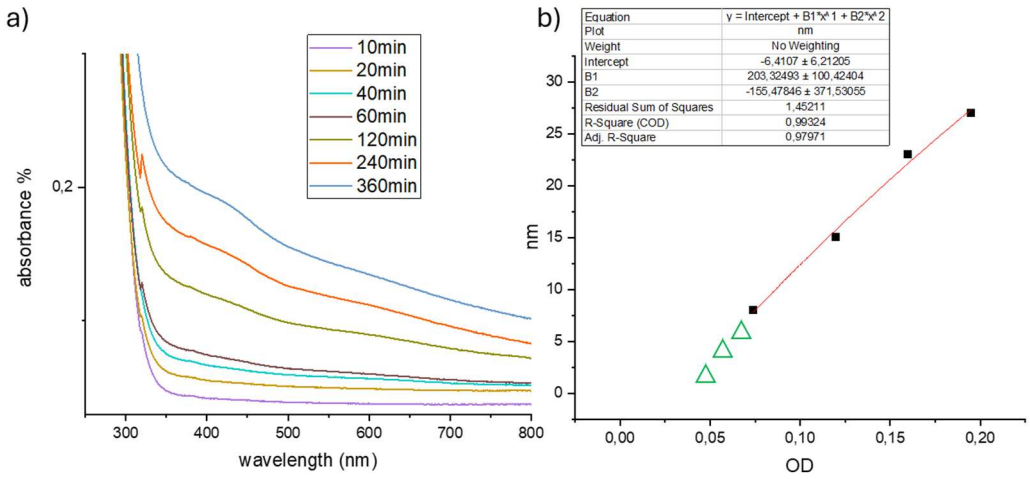

Figure S1.4. a) UV–vis absorption spectra of PDA films grown on glass substrates at various polymerization times (10min-4h). b) Polynomial fitting of optical density values at 400 nm versus AFM-measured thickness for films polymerized between 60 and 360 minutes (fitting equation shown in the inset). Thickness values for shorter polymerization times (10–40 minutes), which could not be reliably measured by AFM due to instrument limitations and surface roughness, were extrapolated using the fitting equation and are shown as green triangles.

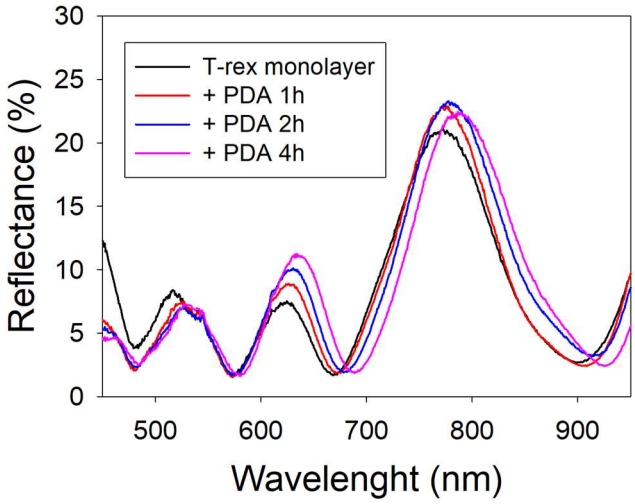

Figure S1.5. Reflectance spectra, in the visible range, of T-rex monolayer substrates incubated with dopamine hydrochloride solution for different time.

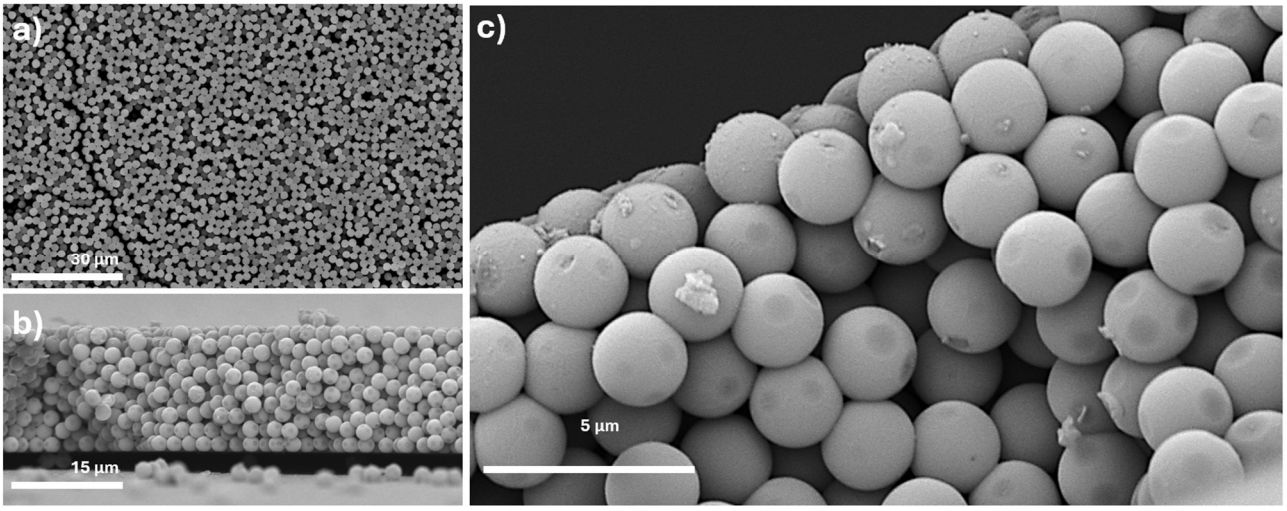

Figure S1.6. SEM images of T-rex multilayers. a) Top view of multilayer T-rex; b) Section view of multilayer T-rex after 4 h of incubation with dopamine hydrochloride. c) Magnified view of the same sample; PDA aggregates attached to the first 3-4 layers of microspheres are visible.

S2. Enhancement factor calculations

A first evaluation of the efficiency of a SERS substrate during the detection of an analyte can be pursued by comparing the intensity of the Raman spectra obtained in the presence and in the absence of the SERS substrate. As an example, in **Figure S2** we compared the spectrum of a MB 10^{-3} M deposited directly on a Si substrate and analyzed with an acquisition time equal to 20s using a 633nm laser, and the spectra of MB 10^{-4} M solution deposited on a T-rex monolayer and a PDA 2h-Trex monolayer, considering the same acquisition conditions.

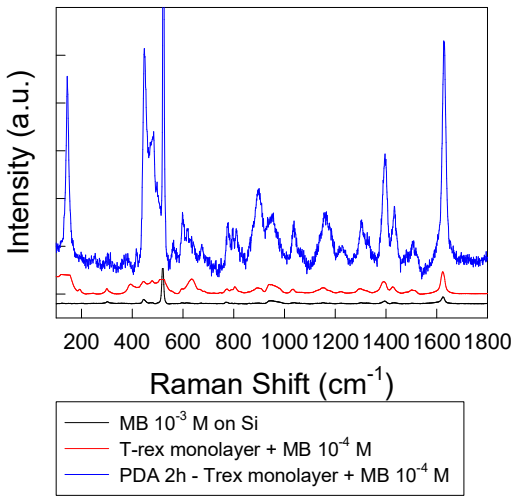

Figure S2. Comparison between the Raman spectrum of a MB 10^{-3} M deposited directly on a Si substrate and analyzed with an acquisition time equal to 20s using a 633nm laser, and the spectra of MB 10^{-4} M solution deposited on a T-rex monolayer and a PDA 2h-Trex monolayer, considering the same acquisition conditions.

From a mathematical point of view, the efficiency of a SERS substrate during the detection of an analyte can be pursued thanks to the calculation of the analytical enhancement factor according to the formula

$$AEF = \frac{I_{SERS}/c_{SERS}}{I_{Raman}/c_{Raman}}$$

where I_{SERS} and I_{Raman} are the intensity of a specific peak for SERS and normal Raman measurements, while C_{SERS} and C_{Raman} are the concentration of the solution used for SERS and Raman analysis (in the same experimental conditions), respectively. Considering the peak at 1620 cm^{-1} and C_{Raman} equal to 10^{-3}M and C_{SERS} equal to 10^{-5}M, an average analytical enhancement factor equal to 22 was obtained for pristine T-rex monolayer, and equal to 747 for the PDA 2h-Trex monolayer.

Of course, the intensity resulting from normal Raman experiments is contributed by a larger number of molecules in comparison to those probed under SERS conditions, since the last one is a mere surface-effect. It drastically decreases moving away from the substrate surface and it is relevant only within 10-20 nm from the SERS substrate surface. As discussed by Le Ru et al. [1], a more accurate evaluation of the enhancement factor should account for the ratio between the number of molecules probed in a SERS experiment and those of the corresponding reference sample. For these reasons, calculating the SERS substrate enhancement factor (SSEF) is more appropriate. SSEF can be calculated according to the formula

$$SSEF = \frac{I_{SERS}/N_{Surface}}{I_{Raman}/N_{Raman}}$$

where N_{Raman} corresponds to the average number of molecules in the scattering volume, during a normal Raman experiment and can be calculated as the product between the bulk molecule concentration (10^{-3} M) and the scattering volume for the normal Raman measurement, multiply for the Avogadro number. This scattering volume is defined as

$$V = \pi r^2 h$$

where the radius r is calculated as

$$r = \frac{0.61\,\lambda}{N.A.}$$

with λ corresponding to the wavelength used for the analysis and N.A. corresponds to the microscope objective numerical aperture. For these measurements N. A. = 0.9.
Instead, h corresponds to the depth of focus, calculated as follows

$$h = \frac{2\lambda}{(N.A.)^2}$$

$N_{surface}$ instead is the number of molecules which can directly participate in a SERS experiment, that correspond to the MB molecules directly adsorbed on the T-rex or PDA 2h-Trex substrates. In fact, SERS effect has been demonstrated to undergo an exponential decay as a function of distance from the SERS-active surface and vanishes within 10-15 nm

So, for the calculation of $N_{surface}$ we considered only the molecules that can be contained inside the volume described by an overcoating shell surrounding the T-rex surface, with a thickness of 15 nm. In the case of SERS experiments we calculated a total scattering volume of 8.05 x 10^8 nm^3, which can contain up to $4.85\ 10^6$ molecules of a MB solution 10^{-5} M.

Using this value as $N_{surface}$ and a value of 5.44 10^8 molecules for $N_{Raman,}$ we obtained an enhancement factor equal to 25 for pristine T-rex monolayer and 840 for PDA 2h-Trex monolayer.

Comparison with plasmonic SERS substrates

SERS substrate	Enhancement factor	Detection limit	reference
$Mo_2CT_x/Fe_2O_3/Ag$	1.46×10^6	1×10^{-9} M	[2]
Spin-Coated Ag NPs	~ 10^9	10^{-10} M	[3]
Electrochemically Synthesized AuNPs	4.4×10^7	9×10^{-11}	[4]
Electrochemically Synthesized AgNPs	1.98×10^9	5×10^{-12}	[4]
AgNPs on anodic aluminum oxide	1.71×10^4	5.10^{-8} M	[5]
3D microporous graphene foam decorated with AgNPs	5×10^4	10^{-9} M	[6]
silver nanocaps	4.2×10^7	-	[7]
gold nanorod@SiO_2	3.0×10^{10}	-	[8]
NaCl activated Ag colloids	-	23×10^{-11}	[9]
Ag NPs on ZnO nanoplates	6.2×10^6	10^{-9} M	[10]
MWCNTs-Ag nanocomposite	4.68×10^6	1 ppm	[11]
Au Nanoworms conjugated with MoS_2 thanks to PDA	~ 10^7	-	[12]
AgNPs + PDA	-	$2.5\ 10^{-8}$ M	[13]
Hydrophobic Cellulose filter paper+ PDA + AgNPs	-	10^{-7} M	[14]
T-rex monolayer	25	10^{-5} M	This work
PDA 2h-Trex monolayer	840	10^{-6} M	This work

Table S1. Enhancement factor and detection limit typical values obtained using plasmonic SERS substrates for the detection of Methylene Blue and comparison with the non-plasmonic substrates described in this work.

S3. PDA-induced variation of wettability

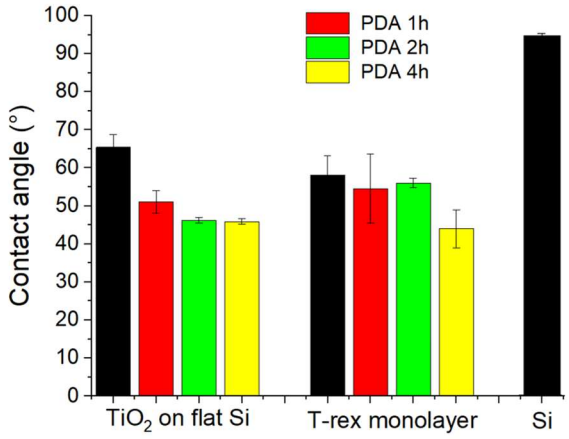

Figure S3. Contact angle of Si-wafer coated with TiO_2 and T-rex monolayer substrates before and after the coverage with PDA layer at different times of growth.

S4. Comparison between monolayer and multilayer substrates

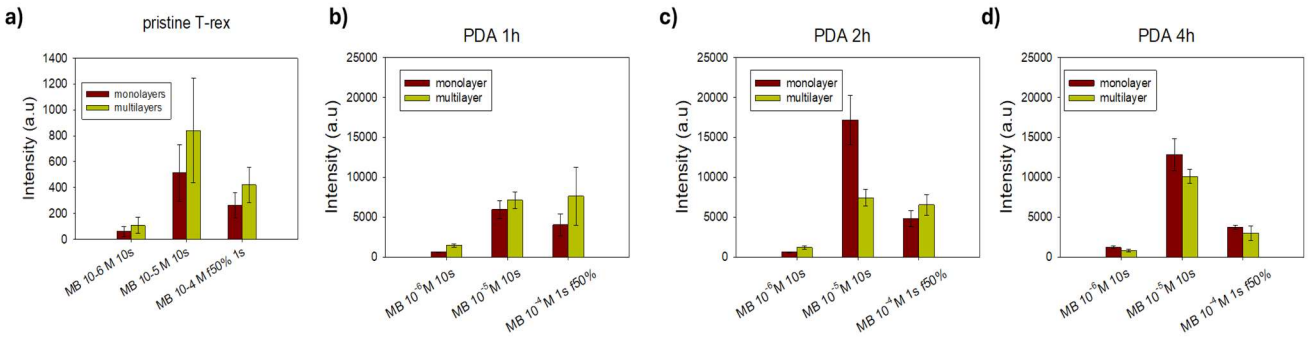

Figure S4. Comparison between the intensity of MB (at different concentrations) peak at 1620 cm^{-1} between monolayer and multilayer substrates. a) pristine T-rex substrates; b) PDA 1h-Trex substrates; c) PDA 2h-Trex substrates; d) PDA 4h-Trex substrates.

S5. Assessment of PDA 2h – Trex monolayer's uniformity, long-term stability, and reusability

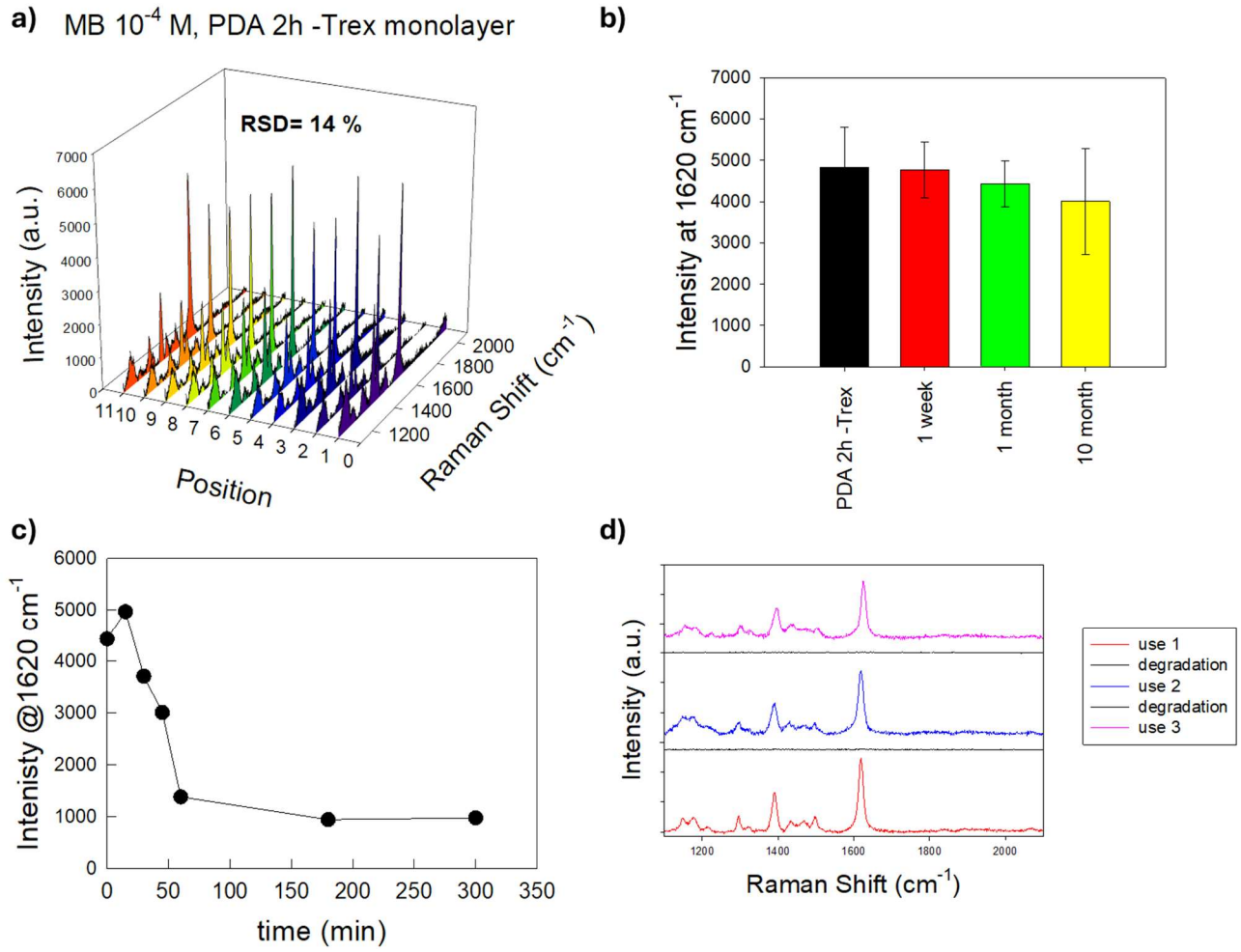

Figure S5. a) Comparison between the Raman spectra of a MB 10^{-4} M solution recorded in 11 different points inside the same PDA 2h – Trex monolayer substrate; b) variation over the time (up to 10 month in standard storage conditions, i.e., ambient temperature and atmosphere, no laser exposure) of the intensity of the main MB peak (for a MB 10^{-4} M solution, acquisition time 1s, f50%) recorded on a same PDA 2h – Trex monolayer substrate in different moments; c) variation over the time (under intermittent laser exposure) of the intensity of the main MB peak (for a MB 10^{-4} M solution, acquisition time 1s, f50%) recorded on a PDA 2h – Trex monolayer substrate; d) reuse of a PDA 2h – Trex monolayer substrate for three consecutive cycles of MB 10^{-4} M detection.

S6. Peak assignment of histamine in normal Raman spectrum

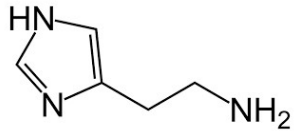

Raman Shift (cm-1)	Assignment
1107	imidazole C-H in-plane bending
1170	imidazole N-H in-plane bending NH_2 rocking
1231	imidazole C-H in-plane bending
1275	imidazole ring stretching
1323	methylene twisting
1359	imidazole ring stretching
1386	methylene wagging
1443	Imidazole ring stretching(CN), imidazole ring bending(NH)
1498	imidazole ring stretching
1570	imidazole ring stretching (C=C)
1593	imidazole ring stretching

Table S2. Peak assignment of histamine in normal Raman spectrum based on references [15–17].

S7. Density Functional Theory (DFT) simulations of the interactions between histamine and TiO_2 and PDA

Polymerization of dopamine into polydopamine (PDA) can result in various configurations, characterized by different monomers and different arrangements. [18] Consequently, selecting a representative model becomes challenging, necessitating an extensive study across multiple geometries. In this study, however, an exhaustive investigation into PDA-histamine interactions is deemed unnecessary, as evidence of favorable adsorption provides a theoretical basis for experimental characterization. The monomer selected for this study is the quinone one, which was chosen for its computational efficiency due to its lower number of atoms compared to alternative structures.

All the Density Functional Theory (DFT) simulations presented in this work were conducted with Quantum Espresso as the periodic nature of plane-waves (PW) helps in representing infinite replicas of a single or a group of monomers [19–22]. The Perdew-Burke-Ernzerhof (PBE) functional within the Generalized Gradient Approximation (GGA) was employed for a balanced trade-off between accuracy and complexity [23]. Convergence tests included optimizing atomic positions along the x-direction (the bonding direction of monomers), with other directions set at arbitrarily large values to prevent mirror interactions (y = 1.5 nm, z = 1.0 nm).

Convergence was achieved when the total energy stabilized within 10^{-4} Ry/atom upon increasing the wavefunction cutoff energy to 5 Ry, using Ecutwfc = 75 Ry and a regular (3, 1, 2) Monkhorst-Pack k-point grid. The PDA surface was constructed by enlarging the supercell to accommodate four monomers, with dimensions adjusted to (1.78, 1.70, 1.70) nm and utilizing the Γ-point to speed up convergence.

Three configurations were investigated: (a) four monomers with identical orientation, (b) three monomers aligned and one rotated (and optionally horizontally flipped, referred to as b*), and (c) a sequence of four

monomers each rotated by 180° with respect to the previous one (*see* **Figure S6**). The formation energy per monomer was calculated as

$$(TE_4 - TE_1) / 4,$$

where TE_4 and TE_1 represent the total energy of the surface (four monomers) and the single monomer, respectively. The obtained results are: –54 kJ/mol for the (a) configuration, -69 kJ/mol for the (b) configuration, –75 kJ/mol for the (b*) configuration and –95 kJ/mol for the (c) configuration.

All the considered PDA configurations are characterized by a negative formation energy, suggesting their stability. However, they differ for the number of H-bonds that can arise between the different monomers inside each structure, which determine the different absolute value of formation energy. In particular, configurations (a), (b) and (b*) are characterized by a lower number of intra structure H-bonds in comparison to configuration (c), which is characterized by a greater proximity between hydrogen and oxygen atoms. This fact leads to a higher availability of H atoms for the formation of new H-bonds with an adsorbate (i.e. histamine) in the case of the (a), (b) and (b*) configurations and it clearly reflects on the strength of the interaction with histamine.

The adsorption energy for histamine was calculated as

$$TE_{PDA+his} - TE_{PDA} - TE_{his},$$

where TE_{PDA} corresponds to TE_4, TE_{his} is the total energy for a histamine molecule in the supercell containing four monomers and $TE_{PDA+his}$ is the total energy for adsorption configuration.

The obtained values are: -45 kJ/mol for the (a) configuration, -45 kJ/mol for the (b) configuration, – 48 kJ/mol for the (b*) configuration and – 29 kJ/mol for the (c) configuration.

In **Figure S7** the adsorption configurations of histamine on different PDA surfaces are represented.

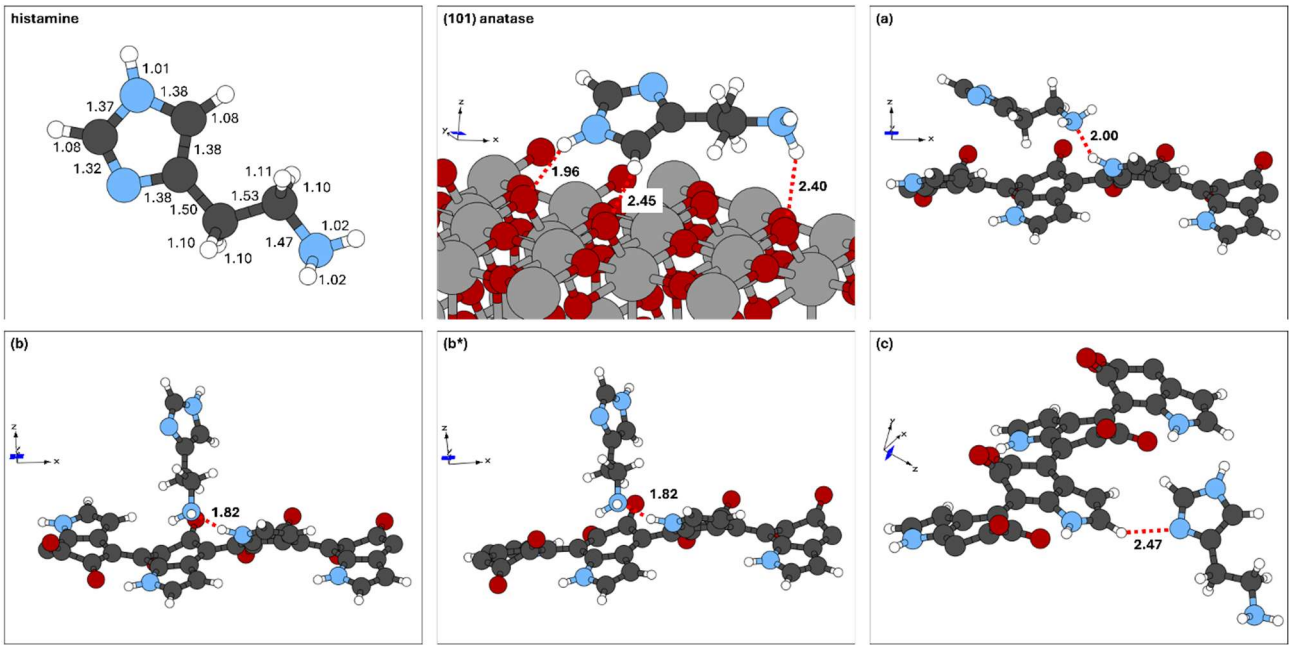

Figure S7. Optimized structures for the free histamine molecule and histamine adsorbed on a TiO_2 surface or on different PDA surfaces. A description of the considered PDA structures can be found in the text. Dotted-red lines indicate proposed H-bonds between molecule and surface. Atom distances in histamine molecules and H-bond lengths are reported in Ångström

For a comparison, a (101) anatase surface was modelled with dimensions similar to those used for PDA, including four vertical layers of titanium atoms, with the bottom two fixed and a vacuum layer of

approximately 1.6 nm added above the slab. This surface is characterized by a formation energy equal to + 50 kJ/mol.

The absorption energy of histamine over this surface is -37 kJ/mol, with three proposed possible interactions between hydrogen atoms of the histamine and oxygen atoms of the surface. Each one of these bonds is characterized by a significantly lower energy respect to H-bonds obtained for the four PDA configurations, leading to a less favourable adsorption.

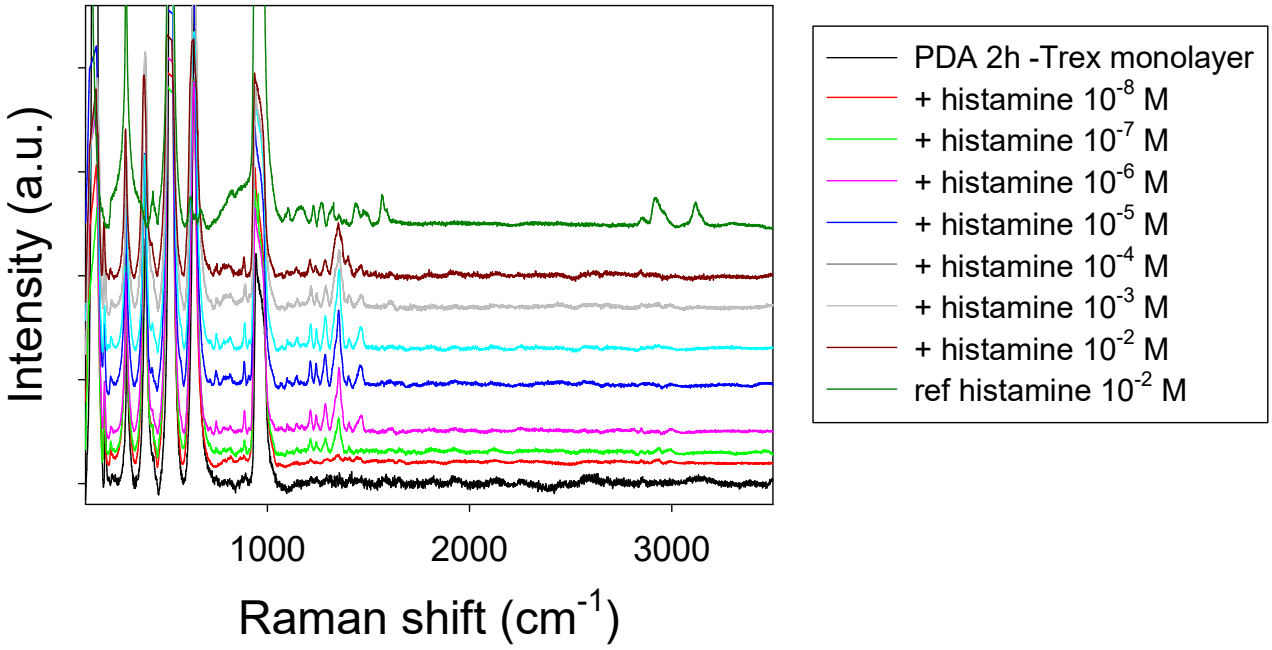

Figure S8. Extended spectra of histamine (10^{-8}-10^{-2}M) using PDA 2h -Trex monolayer as SERS substrate and comparison with the conventional Raman spectrum of a concentrated (10^{-2} M) histamine solution on a Si substrate. Acquisition time 30s.

Bibliography

[1] E.C. Le Ru, E. Blackie, M. Meyer, P.G. Etchegoin, Surface Enhanced Raman Scattering Enhancement Factors: A Comprehensive Study, J. Phys. Chem. C. 111 (2007) 13794–13803.

[2] M. Sakir, E.T. Akgul, M. Demir, Highly sensitive detection of cationic pollutants on molybdenum carbide (MXene)/Fe2O3/Ag as a SERS substrate, Mater. Today Chem. 33 (2023) 101702. https://doi.org/10.1016/j.mtchem.2023.101702.

[3] I. Shaikh, M.A. Haque, H. Pathan, S. Sartale, Spin-Coated Ag NPs SERS Substrate: Role of Electromagnetic and Chemical Enhancement in Trace Detection of Methylene Blue and Congo Red, Plasmonics. 17 (2022) 1889–1900. https://doi.org/10.1007/s11468-022-01671-2.

[4] M.Q. Doan, N.H. Anh, N.X. Quang, N.X. Dinh, D.Q. Tri, T.Q. Huy, A.T. Le, Ultrasensitive Detection of Methylene Blue Using an Electrochemically Synthesized SERS Sensor Based on Gold and Silver Nanoparticles: Roles of Composition and Purity on Sensing Performance and Reliability, J. Electron. Mater. 51 (2022) 150–162. https://doi.org/10.1007/s11664-021-09228-5.

[5] N. Nuntawong, M. Horprathum, P. Eiamchai, K. Wong-Ek, V. Patthanasettakul, P. Chindaudom, Surface-enhanced Raman scattering substrate of silver nanoparticles depositing on AAO template fabricated by magnetron sputtering, Vacuum. 84 (2010) 1415–1418. https://doi.org/10.1016/j.vacuum.2009.12.020.

[6] C. Srichan, M. Ekpanyapong, M. Horprathum, P. Eiamchai, N. Nuntawong, D. Phokharatkul, P. Danvirutai, E. Bohez, A. Wisitsoraat, A. Tuantranont, Highly-Sensitive Surface-Enhanced Raman Spectroscopy (SERS)-based chemical sensor using 3D graphene foam decorated with silver nanoparticles as SERS substrate, Sci. Rep. 6 (2016) 1–9. https://doi.org/10.1038/srep23733.

[7] G.N. Xiao, S.Q. Man, Surface-enhanced Raman scattering of methylene blue adsorbed on cap-shaped silver nanoparticles, Chem. Phys. Lett. 447 (2007) 305–309. https://doi.org/10.1016/j.cplett.2007.09.045.

[8] S.H. Seo, B.M. Kim, A. Joe, H.W. Han, X. Chen, Z. Cheng, E.S. Jang, NIR-light-induced surface-enhanced Raman scattering for detection and photothermal/photodynamic therapy of cancer cells using methylene blue-embedded gold nanorod@SiO2 nanocomposites, Biomaterials. 35 (2014) 3309–3318. https://doi.org/10.1016/j.biomaterials.2013.12.066.

[9] J.A. Anastasopoulos, A. Soto Beobide, A.C. Manikas, G.A. Voyiatzis, Quantitative surface-enhanced resonance Raman scattering analysis of methylene blue using silver colloid, J. Raman Spectrosc. 48 (2017) 1762–1770. https://doi.org/10.1002/jrs.5233.

[10] T.T.H. Pham, X.H. Vu, N.D. Dien, T.T. Trang, T.T.K. Chi, P.H. Phuong, N.T. Nghia, Ag nanoparticles on ZnO nanoplates as a hybrid SERS-active substrate for trace detection of methylene blue, RSC Adv. 12 (2022) 7850–7863. https://doi.org/10.1039/d2ra00620k.

[11] N.X. Dinh, T.Q. Huy, L. Van Vu, L.T. Tam, A.T. Le, Multiwalled carbon nanotubes/silver nanocomposite as effective SERS platform for detection of methylene blue dye in water, J. Sci. Adv. Mater. Devices. 1 (2016) 84–89. https://doi.org/10.1016/j.jsamd.2016.04.007.

[12] H. Yuan, S. Yu, M. Kim, J.E. Lee, H. Kang, D. Jang, M.S. Ramasamy, D.H. Kim, Dopamine-mediated self-assembled anisotropic Au nanoworms conjugated with MoS2 nanosheets for SERS-based sensing, Sensors Actuators B Chem. 371 (2022) 132453. https://doi.org/10.1016/j.snb.2022.132453.

[13] S. Schiavi, A. Taglietti, A. Magni, P. Galinetto, B. Albini, Increasing SERS performance of silver nanoparticles with nanometric coating of polydopamine: A novel approach for methylene blue detection, Appl. Surf. Sci. 687 (2025) 162223. https://doi.org/10.1016/j.apsusc.2024.162223.

[14] J. Dong, T. Wang, E. Xu, F. Bai, J. Liu, Z. Zhang, Flexible Hydrophobic CFP@PDA@AuNPs Stripes for Highly Sensitive SERS Detection of Methylene Blue Residue, Nanomaterials. 12 (2022) 1–13. https://doi.org/10.3390/nano12132163.

[15] K. Kodchakorn, P. Nimmanpipug, S. Phongtamrug, K. Tashiro, PH-induced conformational changes in histamine in the solid state, RSC Adv. 9 (2019) 19375–19389. https://doi.org/10.1039/c9ra03418h.

[16] F. Gao, E. Grant, X. Lu, Determination of histamine in canned tuna by molecularly imprinted polymers-surface enhanced Raman spectroscopy, Anal. Chim. Acta. 901 (2015) 68–75. https://doi.org/10.1016/j.aca.2015.10.025.

[17] E.S. Kolosovas-Machuca, A. Cuadrado, H.J. Ojeda-Galván, L.C. Ortiz-Dosal, A.C. Hernández-Arteaga, M.D.C. Rodríguez-Aranda, H.R. Navarro-Contreras, J. Alda, F.J. González, Detection of histamine dihydrochloride at low concentrations using raman spectroscopy enhanced by gold nanostars colloids, Nanomaterials. 9 (2019). https://doi.org/10.3390/nano9020211.

[18] J. Liebscher, R. Mròwczynski, H.A. Scheidt, C. Filip, N.D. Hadade, R. Turcu, A. Bende, S. Beck, Structure of Polydopamine: A Never-Ending Story?, Langmuir. 29 (2013) 10539–10548.

[19] P. Giannozzi, O. Baseggio, P. Bonfà, D. Brunato, R. Car, I. Carnimeo, C. Cavazzoni, S. de Gironcoli, P. Delugas, F.F. Ruffino, A. Ferretti, N. Marzari, I. Timrov, A. Urru, S. Baroni, Quantum ESPRESSO toward the exascale, J. Chem. Phys. 152 (2020) 154105.

[20] P. Giannozzi, S. Baroni, N. Bonini, M. Calandra, R. Car, C. Cavazzoni, D. Ceresoli, G.L. Chiarotti, M.

Cococcioni, I. Dabo, A. Dal Corso, S. De Gironcoli, S. Fabris, G. Fratesi, R. Gebauer, U. Gerstmann, C. Gougoussis, A. Kokalj, M. Lazzeri, L. Martin-Samos, N. Marzari, F. Mauri, R. Mazzarello, S. Paolini, A. Pasquarello, L. Paulatto, C. Sbraccia, S. Scandolo, G. Sclauzero, A.P. Seitsonen, A. Smogunov, P. Umari, R.M. Wentzcovitch, QUANTUM ESPRESSO: A modular and open-source software project for quantum simulations of materials, J. Phys. Condens. Matter. 21 (2009). https://doi.org/10.1088/0953-8984/21/39/395502.

[21] P. Giannozzi, O. Andreussi, T. Brumme, O. Bunau, M.B. Nardelli, M. Calandra, R. Car, C. Cavazzoni, D. Ceresoli, M. Cococcioni, others, Advanced capabilities for materials modelling with Quantum ESPRESSO. (arXiv:1709.10010v1 [cond-mat.mtrl-sci]), J. Phys. Condens. Matter. 29 (2017) 465901. http://arxiv.org/abs/1709.10010.

[22] Quantum Expresso, (n.d.). https://www.quantum-espresso.org/ (accessed July 31, 2025).

[23] D.R. Hamann, Optimized norm-conserving Vanderbilt pseudopotentials, Phys. Rev. B - Condens. Matter Mater. Phys. 88 (2013) 1–10. https://doi.org/10.1103/PhysRevB.88.085117.